PAPER

Check for updates

Thermal evolution of cathode materials used in commercial sodium-ion batteries

B. D. K. K. Thilakarathna, [ID] [a] Timothy A. Ablott, [ID] [b] Taren Cataldo, [ID] [ab] Pria Ramkissoon, [ID] [c] Govardhan Sontam [a] and Neeraj Sharma [ID] *[a]

The structural evolution of $Na_xNi_{1/3}Fe_{1/3}Mn_{1/3}O_2$ (NFM) cathodes extracted from commercial 18650 sodium-ion batteries at various states of charge, fully charged (FC), partially charged (PC), and fully discharged (FD) is explored. X-ray absorption spectroscopy (XAS) performed at room-temperature on extracted samples indicate changes in the structure and oxidation states of all three transition metals across the different states of charge. Variable-temperature X-ray diffraction (XRD) revealed a progression of thermally induced phase transformations from the initial layered O3 ($R\bar{3}m$) and P3 ($R3m$) structures to a secondary O3 phase, followed by the formation of cubic metal oxide and metallic phases ($Fm\bar{3}m$). Thermogravimetric and differential scanning calorimetric analyses show varying degrees of mass loss and significant exothermic activity, particularly in FC samples, associated with structural changes and cathode decomposition as corroborated by variable-temperature XRD under similar atmospheric conditions. Post-thermal treatment scanning electron microscopy-energy dispersive spectroscopy (SEM-EDS) analysis identifies morphological and compositional differentiation, with irregular Mn/Ni-rich particles and Ni/Fe-enriched spherical domains exhibiting oxygen deficiency. These findings provide an overall view of the thermal response and phase evolution of layered NFM cathodes at different electrochemical conditions.

Introduction

The thermal stability and structural evolution of sodium-based cathode materials are critical factors influencing their performance and safety in rechargeable sodium-ion batteries. Recent studies have provided valuable insights into the temperature-dependent behavior of various Na_xTMO_2 (TM = transition metal) compounds, revealing complex phase transitions and degradation mechanisms.[1] For instance, thermal analysis of Na_xVO_2 cathode materials has demonstrated that the $O'3$–$Na_{1/2}VO_2$ and $Na_{0.55}VO_2$ phases undergo irreversible structural transformations, transitioning to the $P'3$ phase at approximately 145 °C and further evolving into a P3 structure upon heating to 270 °C. In contrast, $Na_{2/3}VO_2$ retains its structural integrity up to 145 °C, consistent with prior findings. These phases are typically synthesized through electrochemical sodium extraction from the O3–$NaVO_2$ parent compound, highlighting the interplay between synthesis conditions and thermal stability.[2]

Similarly, differential scanning calorimetry (DSC) studies on α-$NaFeO_2$ (the structural archetype of the O3 structure, where Na is octahedrally coordinated) electrodes have revealed thermal stability up to 450 °C, with a minor exothermic event observed at 380 °C, attributed to the decomposition of the Teflon (PFTE) binder. Electrochemically derived $Na_{0.58}FeO_2$ (extracted electrode) exhibits an exothermic reaction at about 360 °C corresponding to its decomposition which the authors suggest is indicative of the formation of Fe_2O_3. This suggests that α-$NaFeO_2$ may become thermodynamically unstable during desodiation, potentially due to the formation of Fe^{4+}. However, the precise structural changes accompanying these thermal events remain unresolved, underscoring the need for further investigation.[3]

The thermal behavior of P2-type layered oxides, where sodium is prismatically coordinated, have also been studied. For example, P2 $Na_{0.67}MnO_2$ readily absorbs moisture from the atmosphere, leading to the exchange of Na^+ with H^+ and the formation of hydrated $Na_{0.67}MnO_2$. Thermogravimetric analysis (TGA) of the hydrated material reveals multiple thermal events, including dehydration and $NaHCO_3$ decomposition between 70–130 °C, deprotonation of $Na_{0.67-x}H_xMnO_2$ from 130–217 °C, Na_2CO_3 decomposition above 130 °C, and P2 phase "recrystallization" above 483 °C. Interestingly, substituted variants such as P2 $Na_{0.67}Zn_{0.1}Mn_{0.9}O_2$ exhibit a lower "recrystallization"

[a] *School of Chemistry, UNSW Sydney NSW 2052, Australia.*
E-mail: neeraj.sharma@unsw.edu.au

[b] *Australian Nuclear Science and Technology Organisation, New Illawarra Rd, Lucas Heights NSW 2234, Australia*

[c] *Australian Synchrotron, Australian Nuclear Science and Technology Organisation, 800 Blackburn Road, Melbourne Victoria 3168, Australia*

This journal is © the Owner Societies 2025

Phys. Chem. Chem. Phys., 2025, **27**, 25581–25592 | 25581

temperature of 376 °C, suggesting that chemical substitution can significantly influence thermal stability, heat loss and structural transitions. These findings demonstrate that hydrated Na_xMO_2 compounds can be dehydrated through high-temperature annealing, providing a pathway for material regeneration for battery use.[4]

Further insights into the thermal degradation of cathode materials have been obtained through advanced characterization techniques. For instance, real-time transmission electron microscopy (TEM) studies on P2–Na_xCoO_2 (x = 0.52, 0.24, 0.12) have revealed crystallographic, electronic, and morphological changes under thermal stress. Higher voltage-charged samples (e.g., $Na_{0.12}CoO_2$) exhibit reduced thermodynamic stability, decomposing into cobalt oxides (Co_3O_4, CoO) or even metallic Co at elevated temperatures as determined by electron diffraction. Electron energy loss spectroscopy (EELS) analysis further confirms oxygen loss and the reduction of Co^{3+} to Co^{2+}, with metallic Co formation observed at 400 °C. These results highlight the critical role of the charged state and temperature in governing the thermal stability of layered oxide cathodes.[5]

In addition to layered oxides, polyanionic materials such as $Na_2FeP_2O_7$ have also been investigated for their thermal properties. Synchrotron X-ray diffraction (S-XRD) studies reveal that the charged state ($NaFeP_2O_7$) undergoes a phase transition at 560 °C, transforming from the β-phase (triclinic, $P\bar{1}$) to the α-phase (monoclinic, $P2_1/c$). This transition, confirmed by thermogravimetric-differential scanning calorimetry (TG-DSC), is accompanied by an exothermic peak at 564.2 °C without weight loss, indicating a structural rearrangement rather than decomposition.[6] Similar phase transitions have been observed in $Na_{3.32-x}Fe_{2.34}(P_2O_7)_2$ further emphasizing the thermal resilience of pyrophosphate-based cathodes relative to the layered oxides.[7]

The thermal behavior of P2 $Na_{2/3}MnO_2$ cathodes have also been explored, with studies showing that heating electrodes in sealed argon-filled quartz capillaries lead to the formation of sodium fluoride (NaF) and manganese oxides (Mn_3O_4, MnO). These transformations are accompanied by a reduction in the oxidation state of manganese and the loss of the layered structure. Notably, fully discharged electrodes exhibit a distinctly different phase evolution, with orthorhombic and monoclinic phases persisting up to 500 °C before decomposing into NaF and Mn_3O_4. These findings underscore the influence of state of charge on thermal degradation pathways.[8]

Finally, the thermal stability of O3 $NaMn_{1/3}Fe_{1/3}Ni_{1/3}O_2$ has been investigated at various states of charge (SOC: 100%, 50% and 0%). DSC analysis reveals two major exothermic peaks at 350 °C and 445 °C, with the heat flux magnitude increasing significantly at higher SOC along with a minor endothermic event near 160 °C. X-ray diffraction (XRD) confirms structural instability initiating below 300 °C, preceding significant thermal activity. While the 350 °C exothermic peak at 100% SOC corresponds to a phase transformation, consistent with prior literature, this work indicates that the higher-temperature 445 °C exothermic peak appears to be largely independent of SOC.[9] Gas evolution analysis further corroborates major oxygen release beginning around 300 °C, aligning with the observed

phase transitions and highlighting the material's thermal instability at elevated temperatures. The experiment also investigated the effects of the PVDF binder and the electrolyte (1 M $NaPF_6$ in EC:DMC, 1:1 v/v) on the thermal behavior of the cathode material. DSC analysis revealed two characteristic thermal events associated with PVDF: a minor endothermic peak around 160 °C corresponding to melting, and a prominent exothermic peak near 445 °C attributed to thermal decomposition. These features were also observed in the heat flow profile of the cathode material, indicating that PVDF contributes significantly to the second exothermic event in the composite electrode. However, upon the addition of electrolyte, the exothermic peak previously associated with PVDF decomposition was no longer observed in the DSC curve of the electrode.[10]

Collectively, these studies provide a comprehensive understanding of the thermal behavior of sodium-based cathode materials, emphasizing the importance of structural stability, charge state, and chemical composition in determining their temperature-based evolution and indirectly safety in battery applications. This knowledge is critical for the development of thermally robust cathode materials for next-generation sodium-ion batteries.

In this study, we examine the thermal evolution of $Na_xNi_{1/3}Fe_{1/3}Mn_{1/3}O_2$ (NFM) cathodes extracted from commercial sodium-ion cells at distinct electrochemical states: fully charged (FC), partially charged (PC), and fully discharged (FD). To achieve this, X-ray absorption spectroscopy (XAS) was employed to characterize the oxidation states of the transition metals at room temperature. Variable-temperature XRD was used to monitor structural phase transitions upon heating. DSC and TGA were performed to assess thermal reactivity and decomposition profiles, while scanning electron microscopy with energy-dispersive X-ray spectroscopy (SEM-EDS) was used to investigate morphological features and elemental distribution in final compositions after thermal treatment. Together, these techniques provide complementary insights into the relationships among sodium content, redox chemistry, phase stability, and compositional heterogeneity during thermal exposure.

Results and discussion

The elemental composition of the cathode material for all three samples fully charged (FC), partially charged (PC), and fully discharged (FD) was evaluated using energy-dispersive X-ray spectroscopy (EDS), and inductively coupled plasma – optical emission spectrometry (ICP-OES) as summarized in Table S1. Scanning electron microscopy (SEM) images and corresponding EDS elemental mapping for each electrode are presented in Fig. S2–S4. Both EDS and ICP-OES analysis revealed the presence of Mn, Ni, and Fe in an approximately equi-atomic ratio (1:1:1) across all samples. Variations in sodium content were observed from EDS and ICP-OES analysis. The Na compositions (EDS/ICP-OES) in $Na_xNi_{1/3}Fe_{1/3}Mn_{1/3}O_2$ correspond to 1.10(1)/0.852(6), 0.71(6)/0.648(6), and 0.49(3)/0.446(4) for the FD, PC, and FC samples, respectively which can be attributed to
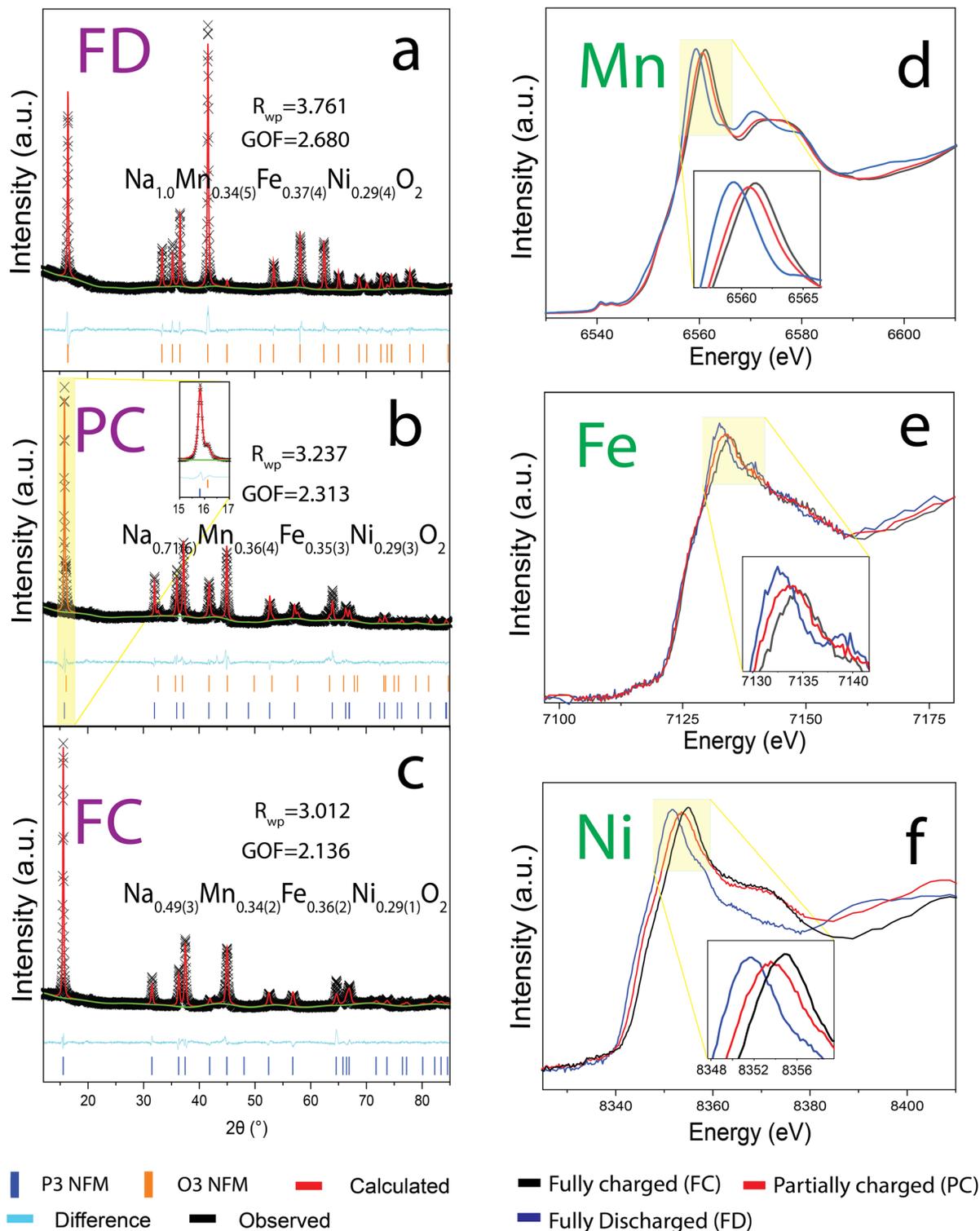
25582 | *Phys. Chem. Chem. Phys.*, 2025, **27**, 25581–25592

This journal is © the Owner Societies 2025

Fig. 1 Rietveld-refined fits of structural models with XRD data (λ = 1.5418 Å) for the $Na_xNi_{1/3}Fe_{1/3}Mn_{1/3}O_2$ (NFM) cathode electrodes extracted at different states of charge: (a) fully discharged (FD), (b) partially charged (PC), and (c) fully charged (FC). Normalized XANES spectra at the (d) Mn (synchrotron source), (e) Fe (lab source), and (f) Ni (lab source) K-edges for the FC, PC, and FD samples. Compositions shown in (a)–(c) are derived from SEM/EDS data.

the expected sodium insertion/extraction (sodiation/desodiation) processes occurring during electrochemical cycling. Fig. 1(a)–(c) shows the Rietveld-refined fits of room temperature XRD data for the NFM cathode electrodes extracted at different states of charge:

(a) FD, (b) PC, and (c) FC. Rietveld analysis of the FD sample was conducted using the O3-type $Na_xNi_{1/3}Fe_{1/3}Mn_{1/3}O_2$ structural model, which adopts $R\bar{3}m$ space group symmetry. In contrast, the FC sample was refined using a P3-type structural model of P3–

$Na_xNi_{1/3}Fe_{1/3}Mn_{1/3}O_2$ adopting $R3m$ space group symmetry. The PC sample exhibited a biphasic character, comprising both O3- and P3-type phases with refined weight fractions of 21.1(4)% and 78.9(4)%, respectively. Room temperature crystallographic parameters including lattice parameters and atomic positions and refinement details, for each distinct phase across the samples are reported in Tables S2–S5.

Fig. 1(d)–(f) presents the normalized *ex situ* X-ray absorption near-edge structure (XANES) spectra collected at the Mn, Fe, and Ni K-edges for the three NFM samples to correlate the oxidation state with state of charge and as shown below as a starting point for discussions around the structures found before heat treatment. Similar XANES data for related structures have been previously reported in several studies[11–13] and in some cases with limited analysis. The XANES of 3d metals show two characteristic regions: a weaker pre-edge region (1s → 3d transitions) and the main absorption edge (convolution of 1s → 4p and 1s → continuum transitions). A shift of the absorption edge toward higher energies typically indicates an increase in oxidation state and the shape of the XANES is highly sensitive to local structure (*e.g.*, coordination, symmetry and donor type) of the absorbing element.[11] Thus, the edge position and shape of the XANES can be used to reveal redox activity and structural changes during electrochemical cycling.[14]

In the Mn K-edge (Fig. 1d), with respect to FC, the absorption edge shifts (~2 eV) towards lower energy in the FD state, suggesting that the Mn in the NFM is evolving as a function of discharge or sodium insertion. Our data is consistent with previously reported data; however, in ref. 12. it was concluded that there was no significant change in the Mn K-edge even with a noticeable shift in the reported data. Upon further consideration, an energy shift is quite clear in Fig. 1d. Furthermore, a distinct change in the shape of the XANES (and onset of the extended X-ray absorption fine structure (EXAFS) region) is also observed from FC to FD, *e.g.*, in the region 6565 to 6585 eV, suggesting a local structural change for the Mn environment during electrochemical cycling. These data, and previously reported data, do in-fact suggest a more substantial change to the redox chemistry and local structure of Mn during cycling.

In the Fe K-edge (Fig. 1e), a shift in the absorption of ~2 eV is also noted during sodium insertion FC to FD, which in this work is from 4.0 to 0.2 V. This observation again closely aligns with the energy shift observed in the previously reported data; however, no change in the Fe K-edge in this voltage range is noted. These works only report changes in the Fe K-edge above 4.0 V[11,12] while the current work notes changes below 4.0 V. It is noted that in $NaFeO_2$, the charge compensation is expected to occur *via* the Fe^{3+}/Fe^{4+} redox couple. However, a study on layered $NaFeO_2$ as a cathode material observed only a small edge shift of ~0.2 eV, suggesting limited Fe oxidation contribution. Moreover, since Na occupies octahedral sites in $NaFeO_2$, some Fe ions can migrate into the alkali-metal layer at high states of charge, creating vacancies in the transition-metal layer. These vacancies may promote oxygen-redox activity, as Fe^{4+} is thermodynamically unstable and can readily reduce back to Fe^{3+}, resulting in a lower apparent absorption-edge energy. Such

behaviour indicates the possible involvement of anionic redox processes during high-voltage operation.[15]

The Ni K-edge (Fig. 1f) shows a more obvious shift (~3 eV) and distinct change in the shape of the XANES data and onset of the EXAFS region from FC to FD. This correlates with previous data[11,12] and demonstrates Ni oxidation/reduction during cycling. In terms of structure, the O3 to P3 transition during charge may in part account for the change in the XANES regions. It is interesting to note distinct changes in the XANES for Ni and Mn. Overall, the XAS results suggest that all three metals (Mn, Ni and Fe) evolve in terms of oxidation state and experience a local structural change during electrochemical cycling.

Fig. S2–S4 show a seemingly bimodal distribution in secondary particles. This distribution likely impacts the thermal evolution as the reactivity between the secondary particles of different sizes may differ and the smaller particles may fuse into larger particles. Fig. 2a and b displays contour plots illustrating the thermal evolution of the (a) (003) and (b) (104) reflections associated with the O3 ($R\bar{3}m$) and P3 ($R3m$) phases in FC, PC, and FD. In the FC sample, the (003) reflection of the P3 phase is prominently observed only up to approximately 300 °C, after which a low-intensity (003) peak corresponding to a O3 ($R\bar{3}m$) phase appears (termed O3-II or secondary O3 and detailed below). This is accompanied by a 2θ shift of approximately 1.0° between the two phases. In contrast, in the FD sample, the (003) peak remains clearly visible up to ~650 °C, although a distinct 2θ shift of nearly 0.1° is observed between 300 °C and 400 °C.
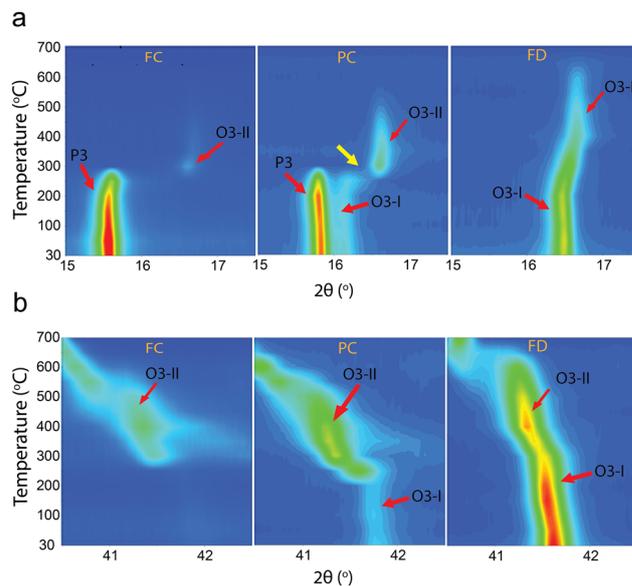

Fig. 2 Contour plots illustrating the thermal evolution of the (a) (003) and (b) (104) Bragg reflections associated with O3- and P3-type layered phases in $Na_xNi_{1/3}Fe_{1/3}Mn_{1/3}O_2$ (NFM) cathode materials, monitored over the temperature range of 30–600 °C. Data were collected using laboratory X-ray diffraction (λ = 1.5418 Å). The temperature-dependent shifts and intensity variations of these reflections highlight structural transitions and phase stability of sodium transition metal oxide phases as a function of temperature across the different electrochemical states.

25584 | *Phys. Chem. Chem. Phys.*, 2025, **27**, 25581–25592

This journal is © the Owner Societies 2025

This behavior suggests two O3 ($R\bar{3}m$) phases, here denoted as O3-I and O3-II. This is confirmed by (104) reflection which appears to show two distinct phases, one decreasing in intensity while the other increases in the FD sample (Fig. 2b).

In the PC sample, both P3 ($R3m$) and O3 ($R\bar{3}m$) type phases coexist at room temperature. The (003) reflection associated with the P3 ($R3m$) phase diminishes around 300 °C, resembling the trend observed in the FC sample. Notably, as in the FD sample, the initial O3-I ($R\bar{3}m$) (003) reflection in the PC sample also fades near 300 °C, with a new O3-II phase emerging around 350 °C. This secondary O3-II ($R\bar{3}m$) phase exhibits distinct segregation from the original O3-I ($R\bar{3}m$) phase and shows a nearly identical 2θ position to that observed in the FD and FC samples.

The emergence of this O3-II ($R\bar{3}m$) phase is further supported by the evolution of the (104) peak intensities associated with these O3-II ($R\bar{3}m$) phases across all samples. The (104) reflection is more pronounced in O3 phases and appears only weakly in P3 ($R3m$) phases, such as in FC. Thus the (104) peak observed in PC up to 250 °C is primarily contributed by the initial O3 ($R\bar{3}m$) phase rather than the P3 ($R3m$) phase. Comparatively, the intensities of the reflections corresponding to the O3-II ($R\bar{3}m$) phases are more prominent in samples with higher sodium content (*e.g.*, FD) than in those with lower sodium content (*e.g.*, PC followed by FC). In other words, the intensity of the O3-II phase is most intense in the FD or high sodium-content samples relative to FC. This is mirrored in Fig. 3, as the O3-II phase shows the highest phase fraction in the FD sample. This implies that sufficient Na content is critical for the formation and thermal stabilization of the secondary O3 ($R\bar{3}m$) phase at elevated temperatures.

The O3-I, O3-II and P3 phases were modelled across the samples, Fig. 3 and Table S6 illustrate the thermal evolution as a function of state of charge. Similar phase evolution occurs across the electrochemical series as a function of temperature, with the formation of a secondary O3-II phase ($R\bar{3}m$), then a cubic transition metal oxide phase ($Fm\bar{3}m$), and a cubic metallic phase ($Fm\bar{3}m$) observed in all samples. Generally, all samples first undergo a transformation to the cubic transition metal oxide phase, followed by/with the formation of the cubic metallic phase. This sequence suggests a reducing environment is available in and around the electrode, wherein the transition metal oxidation states evolve from a mixed +3/+4 state in the initial electrodes to +2 in the metal oxide and eventually to 0 in the metallic phase.

The onset temperatures and stability ranges of these transformations vary depending on the initial state of charge (*i.e.*, sodium content) of the electrodes. In the Na-rich FD sample, the phase evolution begins with the original O3 ($R\bar{3}m$) NFM structure at room temperature, which transitions to a O3-II ($R\bar{3}m$) phase at around 350 °C. Upon further heating, both the cubic transition metal oxide ($Fm\bar{3}m$), and metallic phases ($Fm\bar{3}m$), emerge, and notably, these phases are retained even after cooling to room temperature.

The FC sample (charged state or low sodium content) exhibits the formation of a O3-II ($R\bar{3}m$) at a lower temperature
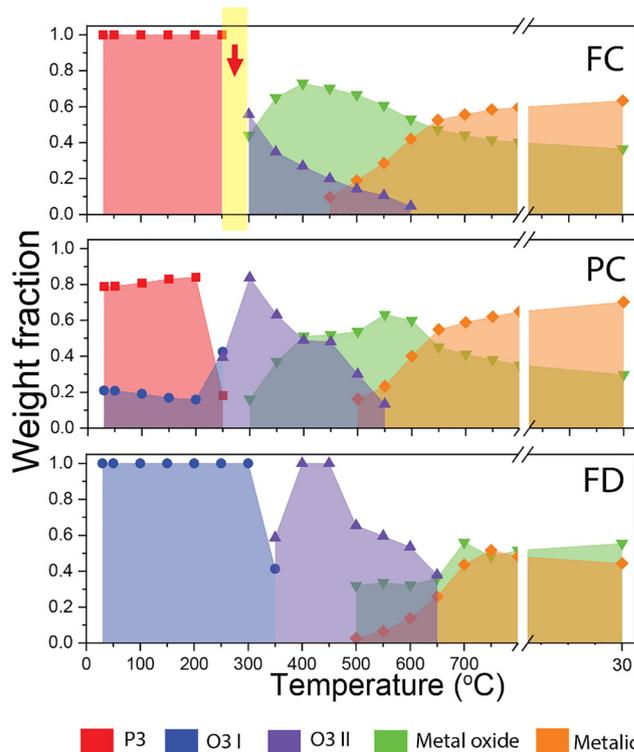

Fig. 3 Thermal phase evolution of Na$_x$Ni$_{1/3}$Fe$_{1/3}$Mn$_{1/3}$O$_2$ (NFM) cathode materials at different states of charge: fully charged (FC), partially charged (PC), and fully discharged (FD). Phase weight fractions were quantified as a function of temperature using Rietveld refinement of structural models with variable temperature X-ray diffraction data. The analysis reveals distinct temperature–dependent phase transformations and thermal stability differences as a function of electrochemical state.

($\sim$250–300 °C indicated by red arrow in Fig. 3) compared to the FD sample. The PC sample, with intermediate sodium content, initially displays both P3 and O3 phases. At approximately 250 °C, a phase transition occurs to a O3-II ($R\bar{3}m$) phase similar to that observed in FC. The initial P3/O3 weight fraction in the PC sample is 0.789(4)/0.211(4), which likely explains the similarity in phase evolution between PC and FC, both being dominated by the P3-type characteristics. Overall, these results highlight that the sodium content (state of charge) influences the subsequent thermal phase evolution. Selected Rietveld refinements depicting the structural evolution for each sample are shown in Fig. S5.

Up to the phase transition point in the PC sample, 200 °C, the P3/O3 weight fraction remains nearly constant, with a preference for the P3 ($R3m$) phase over the O3 ($R\bar{3}m$) phase. In the FD sample, the O3-II ($R\bar{3}m$) phase becomes predominant between $\sim$400–600 °C, although its fraction starts to decline from approximately 450 °C. In contrast, decrease of the O3-II phase begins at $\sim$300 °C in both the FC and PC samples, and it is the prevalent phase over a narrower temperature range compared to the FD sample. This trend indicates that higher sodium content promotes the formation of and a longer temperature range of existence of the O3-II type ($R\bar{3}m$) NFM phase. Conversely, the limited or suppressed formation of this

This journal is © the Owner Societies 2025

Phys. Chem. Chem. Phys., 2025, **27**, 25581–25592 | **25585**

phase in the PC and FC samples correlates with the earlier emergence of transition metal oxide phases, which begin to form around ∼300 °C in both FC and PC, compared to ∼500 °C in FD. These de-sodiated cubic transition metal oxide phases (space group $Fm\bar{3}m$) dominate the phase fractions between 350–600 °C in the FC sample and 400–600 °C in the PC sample, whereas they remain a minor component in the FD sample over the same temperature range. The high-temperature formation of transition metal oxide and metallic phases from sodium transition metal oxides has been previously reported.[5] This observation further underscores the critical role of sodium content in governing thermal decomposition pathways, where a higher initial sodium content delays and mitigates the formation of sodium-deficient phases during heating. Note, trace amounts of trapped electrolyte may influence the chemical transformations, particularly below ∼300 °C.[16]

The disappearance of the sodiated O3-II ($R\bar{3}m$) phase occurs around 650 °C in the FD sample, whereas in the FC and PC samples, it vanishes at significantly lower temperatures. The cubic metallic phase first emerges in the FC sample at approximately 450 °C, followed by its appearance in the PC and FD samples at around 500 °C. Overall, the formation of sodium-free cubic transition metal oxide and metallic phases were delayed in Na-rich samples and occurred earlier in Na-deficient samples. At higher temperatures (especially >650 °C), the dominance of the metallic phase is most pronounced in the FC and PC samples. This trend further supports the observation that initial sodium content governs not only the onset but also the extent of high-temperature phase transformations. For instance, at 750 °C, the FC sample exhibits significantly higher metallic phase content, reinforcing the conclusion that sodium content critically influences the phase evolution of NFM cathodes under high temperature conditions.

Fig. 4 and Tables S7–S9 presents the evolution of the lattice parameters for the P3 and both O3 phases observed in the FC, PC, and FD samples. The original P3 ($R3m$) and O3 ($R\bar{3}m$) phases exhibit a relatively gradual increase in both a and c lattice parameters during the thermal evolution (with the exception of 250 °C for the c lattice parameter in some cases). Except for the P3 phase in the FC sample, all the initial layered sodium metal oxide phases exhibit generally similar volume expansion, and the lattice parameters and volume expansion coefficients are shown in Tables S12 and S13. The maximum thermal expansion coefficient is observed in the FC P3 ($R3m$) phase, with a value of $53(20) \times 10^{-5}$ °C^{-1} between 30 and 250 °C. The sharp expansion occurring between 200 °C and 250 °C in this sample is primarily responsible for the relatively large associated error in the calculated thermal expansion coefficient. Notably, at approximately 250 °C, the a lattice parameter undergoes a sudden increase across all samples, whereas the c lattice parameter exhibits a decrease compared to its value at 200 °C for the original O3 ($R\bar{3}m$) phases. Correspondingly, the unit cell volume shows an inflection between 200 and 250 °C displaying a more pronounced increase above this range and therefore different to thermal expansion of the original O3 ($R\bar{3}m$) phases. This abrupt variation in a lattice parameter and unit cell volume near 200 °C could stem from
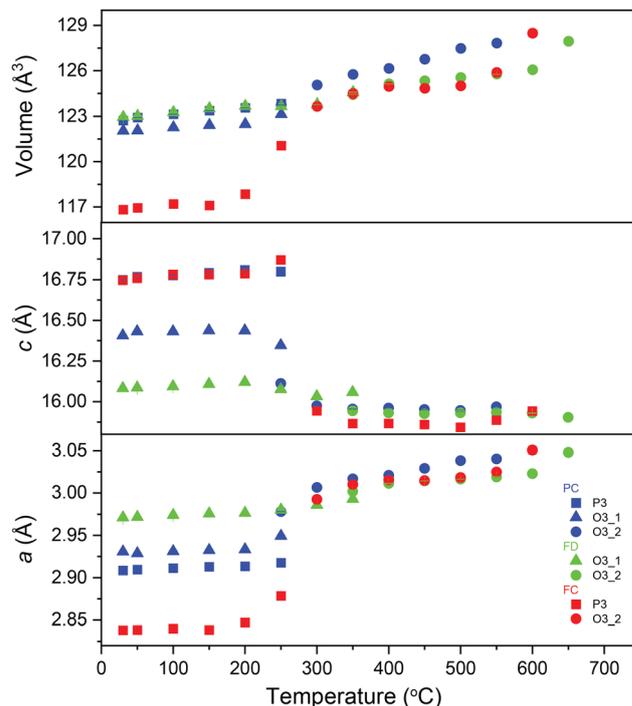

Fig. 4 Temperature-dependent evolution of lattice parameters (a) and (c) and unit cell volume for the O3 ($R\bar{3}m$) – and P3 ($R3m$) – type phases identified in Na$_x$Ni$_{1/3}$Fe$_{1/3}$Mn$_{1/3}$O$_2$ (NFM) cathode materials across fully charged (FC), partially charged (PC), and fully discharged (FD) states. The structural parameters were extracted from sequential Rietveld refinements using structural models with high-temperature X-ray diffraction data over the range of 30–650 °C.

several contributing factors: intrinsic thermal expansion or contraction, the initiation of a phase transformation – most plausibly the emergence of a O3-II ($R\bar{3}m$) phase – and/or changes in the sodium content within the original phase.

The O3-II ($R\bar{3}m$) phase emerges between 250–650 °C. Across all samples, comparable lattice parameters are observed for this phase, e.g., at 450 °C, indicating the formation of structurally and compositionally similar phases. This O3-II ($R\bar{3}m$) phase demonstrates general stability in its c lattice parameter, alongside a progressive increase in the a lattice parameter and overall unit cell volume. Among the samples, the PC sample exhibits a comparatively greater expansion coefficient in both the a lattice parameter ($70.5(2) \times 10^{-6}$ °C^{-1}) and volume expansion coefficient ($10.5(8) \times 10^{-5}$ °C^{-1}) than the corresponding O3-II ($R\bar{3}m$) phases found in the FD and FC samples. However, the thermal expansion behavior of the c lattice parameter remains generally consistent across all cases.

Fig. 5 and Tables S10, S11 present the evolution of lattice parameters and unit cell volume for the cubic transition metal oxide and cubic metallic phases. These phases are consistently formed across all samples and generally have similar lattice parameters, potentially indicating similar compositions. The cubic transition metal oxide phase generally expands up to ∼650 °C in all cases. There is some evidence of stabilisation of the volume from 650 °C onwards most apparent in the FD sample. In the FD sample there is an increase in the volume
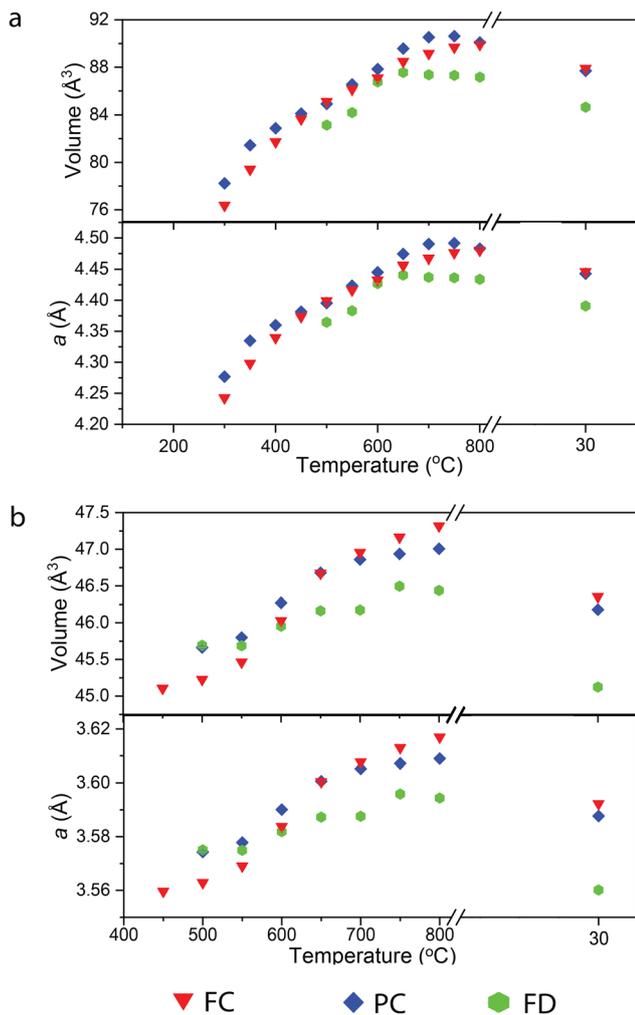
25586 | *Phys. Chem. Chem. Phys.*, 2025, **27**, 25581–25592

This journal is © the Owner Societies 2025

Fig. 5 Temperature-dependent evolution of a lattice parameter and unit cell volume for (a) transition metal oxide and (b) cubic metallic phase identified in $Na_xNi_{1/3}Fe_{1/3}Mn_{1/3}O_2$ (NFM) cathodes at fully charged (FC), partially charged (PC), and fully discharged (FD) states. The data were obtained from sequential Rietveld refinements of structural models with high-temperature X-ray diffraction patterns across the 300–800 °C range.

until 650 °C after which the thermal expansion shows near zero expansion until 800 °C. The volume thermal expansion coefficient for FD between 500–650 °C is $34(6) \times 10^{-5}$ °C^{-1}, while from 650–800 °C it is $-2.5(5) \times 10^{-5}$ °C^{-1}. For the FC and PC samples the thermal expansion coefficient between 350–750 °C is $31(3) \times 10^{-5}$ °C^{-1} and $26(3) \times 10^{-5}$ °C^{-1} respectively. Between 600 °C and 800 °C, the cubic transition metal oxide phase in the PC sample shows the highest unit cell volume ($90.617(12)$ Å^3 at 750 °C), while the lowest is observed in the FD sample ($84.657(6)$ Å^3 at 800 °C).

The cubic metallic phase generally continues to expand throughout the entire heating process, reaching up to 800 °C in all samples. In the FC sample it shows a slight inflexion at 600 °C which may be present in the PC sample. The volume thermal expansion coefficient for FC, PC and FD between 600–800 °C are $10(2) \times 10^{-5}$ °C^{-1}, $67(18) \times 10^{-6}$ °C^{-1} and $57(17) \times 10^{-6}$ °C^{-1} respectively. After 600 °C, the metallic phases in the
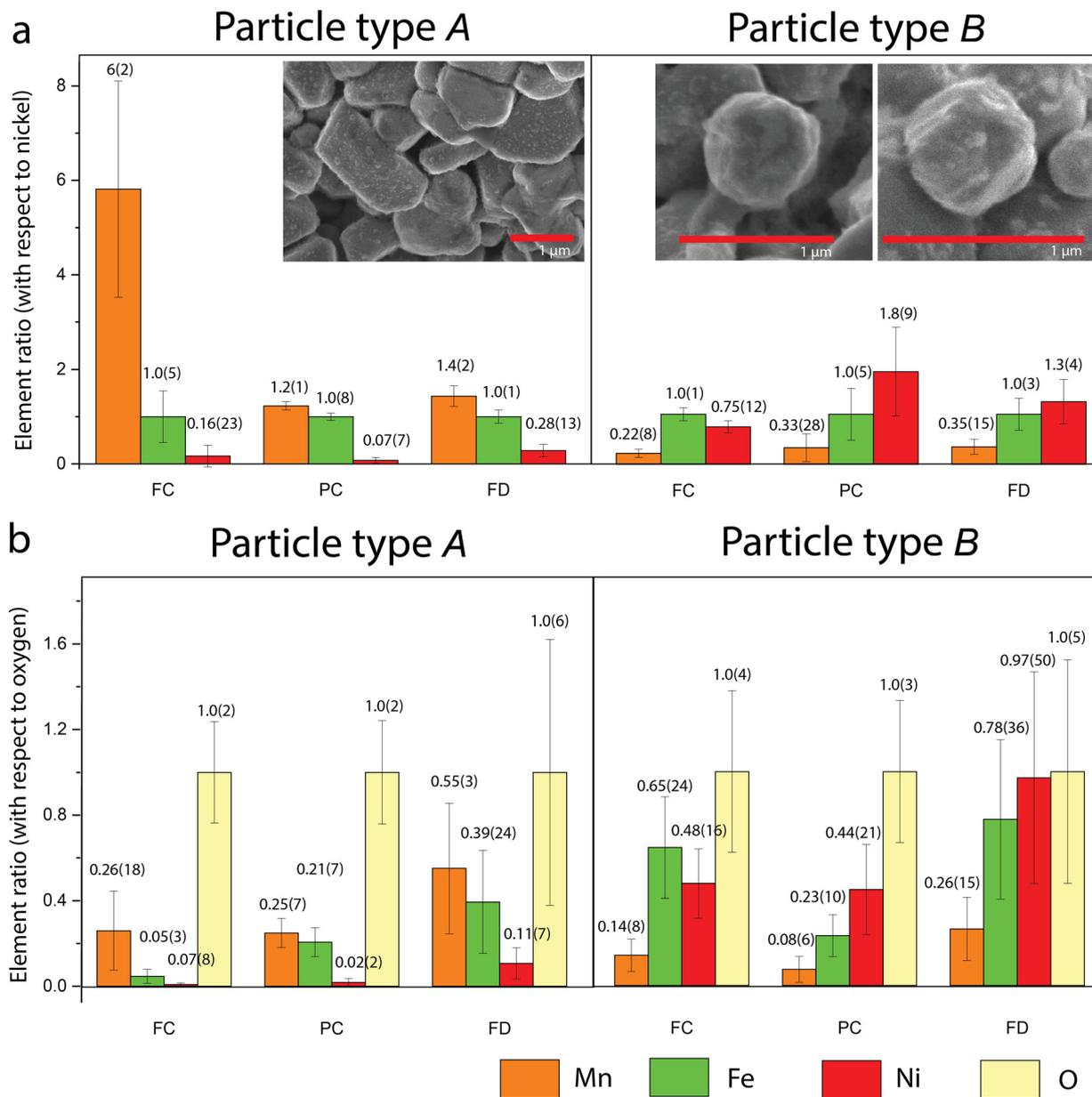
PC and FC samples display larger unit cell volumes compared to that of the FD sample. Notably, both the cubic transition metal oxide and cubic metallic phases are retained after cooling to room temperature (Tables S10 and S11). Furthermore, the FC and PC samples have nearly identical lattice parameters while FD is smaller for both the cubic transition metal oxide and cubic metallic phases after 600 °C. To further elucidate the distinction between the transition metal oxide and metallic phases, a complementary analysis of particle composition and morphology was conducted at room temperature on samples after heat treatment. The divergence in phase evolution and the deviations in lattice parameters between these phases after cooling (see Fig. 3 and 5) suggest potentially subtle differences in their underlying chemistries. Preliminary SEM analysis identified two dominant particle morphologies consistently observed across all samples at the end of the thermal treatment (*i.e.*, after heating and cooling to 30 °C): (a) particle type A: irregular-shaped particles and (b) particle type B: spherical-shaped particles (Fig. 6).

Energy-dispersive X-ray spectroscopy (EDS) analyses (Fig. 6) revealed systematic differences in transition metal distribution between the two particle types. Particle type A was consistently enriched in Mn and Fe, whereas particle type B showed relatively higher concentrations of Ni and Fe. FC sample is interesting as particle type A exhibited a significantly higher Mn-to-Fe atomic ratio of approximately $6(2):1.0(5)$ – a trend not observed in the PC and FD samples. Additionally, particle type B in the FC sample displayed an elevated Fe-to-Ni ratio of $1.0(1):0.75(12)$, again differing from those observed in the PC and FD samples. Overall, these data suggest that the two particle families likely correspond to the transition metal oxide and metallic phases found in the XRD analysis. One of these are Mn/Fe enriched while the other is Ni/Fe enriched.

Fig. 6b highlights the atomic ratios with the inclusion of oxygen for both particle types across all samples. It is important to note that these calculated TM : O ratios do not account for oxygen contributions from non-transition-metal-containing species, such as residual or surface-bound sodium carbonates (*e.g.*, Na_2CO_3). These species may artificially increase the measured oxygen content, especially at the particle surfaces. Further, oxygen determination is not as reliable as transition metal determination with the current EDS experiments. Overall, there is significantly more oxygen detected in particle type A compared to particle type B. This suggests the particle type A is likely to be the transition metal oxide, which suggests that the transition metal oxide is Mn/Fe enriched while particle type B is the metallic species which is Ni/Fe enriched.

To complement the structural analysis, thermal analysis that match the variable temperature XRD experimental approach was undertaken. Fig. 7 illustrates the thermal behavior of the samples illustrating weight loss, heat flow, and their derivatives. The corresponding enthalpy calculations are presented in Fig. S6. Four distinct temperature regions were identified based on the observed thermal events: (1) 75–175 °C, (2) 280–510 °C, (3) 600–730 °C, and (4) >750 °C. The cumulative weight loss increases systematically with the state of charge (SOC), with the

This journal is © the Owner Societies 2025

Phys. Chem. Chem. Phys., 2025, **27**, 25581–25592 | **25587**

Fig. 6 Elemental composition analysis by EDS measurements of particle types identified in $Na_xNi_{1/3}Fe_{1/3}Mn_{1/3}O_2$ (NFM) cathode materials after thermal treatment and cooling to 30 °C. (a) Atomic ratios of Mn, Fe, and Ni normalized to Ni content for particle type A (irregular-shaped) and particle type B (spherical) across fully charged (FC), partially charged (PC), and fully discharged (FD) states. SEM images of both particle types are included as insets to illustrate the particle shape differences. Particle type A consistently exhibits Mn enrichment, while particle type B shows relatively higher Fe and Ni content. (b) Atomic ratios of Mn, Fe, and Ni normalized to oxygen content for both particle types. Particle type A generally exhibits higher oxygen-to-transition-metal (O : TM) ratios, whereas particle type B displays lower O : TM ratios.

FC sample exhibiting the greatest total mass loss, and the FD sample the least. The weight loss across these temperature intervals for each sample is summarized in Table S14. Notably, the FC sample shows significantly higher weight loss rates in regions (1) and (2) compared to the PC and FD samples. While the PC and FD samples exhibit comparable behavior in the 75–175 °C range, the PC sample demonstrates a distinctly higher mass loss rate between 280–425 °C than the FD sample.

The initial mass loss below 175 °C is most likely attributed to the evaporation of residual electrolyte solvents and adsorbed moisture, commonly retained in porous electrode materials. For example, some carbonate-based solvents such as dimethyl ether (DME), 1,1,2,2-tetrafluoroethyl-2,2,3,3-tetrafluoropropyl ether (TTE), and diethyl carbonate (DEC) typically evaporate around 100 °C exhibiting characteristic endothermic features.[17] A previous study on hydrated P2-type $Na_{0.67}MnO_2$ reported dehydration and $NaHCO_3$ decomposition occurring between 70–130 °C.[4] Additionally, thermal events in this region may partially overlap with binder transitions. A study on PVDF, a commonly used binder in sodium-ion cathodes, identified two
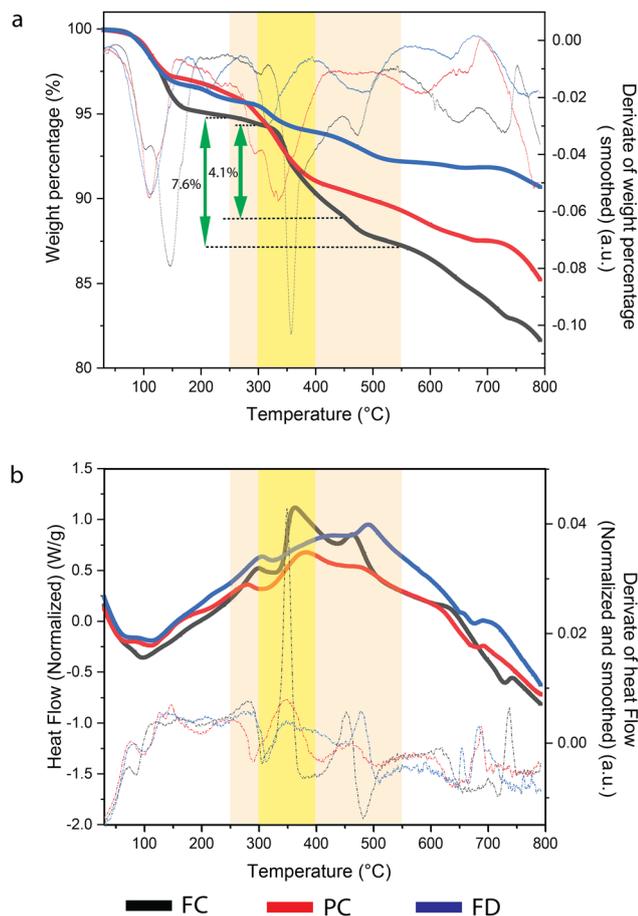
25588 | Phys. Chem. Chem. Phys., 2025, 27, 25581–25592

This journal is © the Owner Societies 2025

Fig. 7 (a) Thermogravimetric analysis (TGA) showing weight percentage (solid lines) and its first derivative (dash lines), and (b) differential scanning calorimetry (DSC) profiles displaying normalized heat flow (solid lines) and its derivative (dash lines), for $Na_xNi_{1/3}Fe_{1/3}Mn_{1/3}O_2$ (NFM) cathode materials at fully charged (FC), partially charged (PC), and fully discharged (FD) states.

key thermal transitions: an endothermic melting event near 163 °C and an exothermic decomposition peak around 450 °C in a He environment.[10] The observed heat flow signals are consistent with these features, suggesting that the secondary exothermic peak below 500 °C may arise from PVDF degradation, assuming PVDF is present in the electrode formulation.

Previous studies on NFM-type cathodes have reported two distinct exothermic peaks near 350 °C and 445 °C. The intensity of the first peak increases with SOC, indicative of greater oxygen evolution and enhanced structural instability in more desodiated states.[10] This trend aligns with our DSC data, wherein the FC sample exhibits the most prominent exothermic peak around 350 °C. Given oxygen is likely evolving from the sample, an increase in the intensity of this DSC peak should be coupled with a greater mass loss in the TG trace. As evident in Fig. 7a, such a trend is observed, with a mass loss of approximately 4.1% in the FC sample, with smaller mass losses in the PC and FD samples. These observations support the hypothesis that a higher charge state elevates the ease of oxygen release of the cathode due to reduced sodium content. This could assist in transition metal reduction to account for oxygen

loss. It should be noted; carbon black is often used as a conductive agent which would also assist in generating a local reductive environment and this could couple with oxygen loss from the active material. TGA-mass spectroscopy would be an excellent tool to use to verify oxygen release or to monitor the gas release during this process.

The pronounced heat evolution and weight loss (*e.g.*, 7.6% in FC) observed between 250–550 °C are consistent with multiple phase transformations and decomposition pathways, as confirmed by variable-temperature XRD analysis. These include the decomposition of sodium-rich transition metal oxides and the formation of sodium-deficient or sodium-free oxide phases, and, in some cases, metallic phases.[3,5,8]

Across all three samples, three principal exothermic events were observed in the DSC traces between 250–500 °C; however, the FC sample exhibits the largest total enthalpy change (155.8 J g^{-1}), compared with 88.3 J g^{-1} for PC and 39.9 J g^{-1} for FD within this temperature range. A previous study using $NaPF_6$ and $NaClO_4$ electrolytes with varying concentrations and combinations of EC, DEC, and DMC solvents reported exothermic events with peak temperatures between 267–302 °C, implying that the exothermic feature observed around 300 °C in all three samples may be contributed by similar electrolyte decomposition processes.[16] As shown in Fig. 7b, the DSC profiles for each SOC reveal exothermic peaks between 300–450 °C, which can be correlated with O3-to-O3 or P3-to-O3 transitions and the development of intermediate oxide structures. Notably, in the 350–400 °C range, the derivative intensity of the heat flow follows the order FD < PC < FC, reflecting the SOC-dependent reactivity. This is reflected in the calculated enthalpies for the major exothermic event, with values of 107.2, 61.3 and 11.4 J g^{-1} for the FC, PC and FD samples, respectively. A similar trend is observed in the mass loss, with the FC sample exhibiting the highest weight loss of approximately 4.1% in this temperature range. Finally, this behavior can be related to the structural transitions that occur in the NFM phase where the FD sample shows an O3–O3 transition while the FC sample shows a P3 to O3 transition. The PC sample exhibits intermediate characteristics as it evolves from a mixed P3/O3 phase composition.

The DSC peaks in the 450–500 °C range are correlated to the phase transitions and the thermal degradation of conductive additives. A study demonstrated that carbon black undergoes two distinct decomposition stages between 270–330 °C and 330–550 °C under an argon atmosphere.[18] In this thermal event, the enthalpy changes were quantified as 29.6 J g^{-1} (FC), 8.9 J g^{-1} (PC), and 21.7 J g^{-1} (FD). The DSC peak attributed to aluminium melting has previously been reported in the range of 659–700 °C. It is possible that trace amounts of aluminium, introduced during the scraping procedure from the current collector, are present in the extracted samples. This may contribute to the thermal features observed in the FD and PC samples within this temperature range.[19] At temperatures above 650 °C, no phase transitions are noted by XRD but minor exothermic features are evident in the DSC traces showing enthalpy changes of 5.4, 2.5, and 7.3 J g^{-1} for FC, PC, and FD, respectively. These may correspond to intra-phase ion

This journal is © the Owner Societies 2025

Phys. Chem. Chem. Phys., 2025, **27**, 25581–25592 | **25589**

exchange, the formation of disordered or amorphous oxide phases, or low-crystallinity products undetectable by conventional XRD due to their limited volume fraction or structural disorder.[20–22] Future work can be directed to identifying the compositions across the various transitions in order to develop reaction equations.

Conclusions

This study presents a comprehensive examination of the thermal evolution of $Na_xNi_{1/3}Fe_{1/3}Mn_{1/3}O_2$ (NFM) cathodes at different states of charge, utilizing variable-temperature X-ray diffraction (XRD) as the primary analytical method, supported by XAS, DSC-TGA, and SEM-EDS. Room-temperature XAS established the initial oxidation states of the transition metals, revealing state of charge dependent variations, involving all three transition metal elements, Ni, Fe and Mn. Variable-temperature XRD identified a consistent sequence of phase transitions: the initial layered O3/P3 structures transformed into a secondary O3 phase, followed by the formation of cubic transition metal oxide and cubic metallic phases, with transitions occurring at lower temperatures in desodiated samples. Complementary DSC–TGA analyses demonstrated variations in thermal reactivity and mass loss that correlated with the structural transformations observed by variable temperature XRD. SEM-EDS analysis, performed on the post-heated and cooled samples, revealed compositional segregation into Mn-rich and Ni/Fe-rich regions, which could plausibly correspond to oxide and metallic phases, respectively, based on the phase evolution pathways determined by XRD. Collectively, these interconnected results contribute to a broader understanding of how sodium content influences the structural, chemical, and thermal behavior of layered oxide cathodes under thermal stress.

Experimental

Commercial 18650 sodium-ion batteries (SIBs) with a nominal capacity of 1500 mAh and a quoted voltage of 3 V were purchased and obtained from HAKADI. Electrochemical cycling was performed between 0.2 V and 4.0 V at a constant current of 1 A. At 4.0 V, a potentiostatic hold was applied until the current declined to 30 mA. During the second cycle (after purchase), three distinct states of charge were selected: fully charged (4.0 V), partially charged (3.0 V), and fully discharged (0.2 V); see Fig. S1. All electrochemical cycling was conducted at room temperature. Following cycling, selected cells were disassembled in an argon-filled glove box. A Dremel tool was used to open the cell casing and extract the jelly roll. Cathode and anode components were then separated for subsequent analysis.

Elemental analysis was performed using a PerkinElmer AVIO-500 DV inductively coupled plasmas optical emission spectrometer (ICP-OES) operated under the following conditions; power $\sim$1500 W; plasma gas flow: 12 L min^{-1}; auxiliary gas flow: 0.4 L min^{-1}; nebulizer gas flow: 0.6 L min^{-1} and controlled with Syngistix software. Yttrium (λ = 371.029 nm)

was used as the internal standard. Calibration was performed using freshly prepared multi-element standards derived from certified stock solutions. A four-point calibration curve was established at 0.2, 1, 10, and 100 mg L^{-1}, including a blank. Standards were prepared in 2% reverse aqua regia (a mixture of 4 parts concentrated HNO$_3$ and 2 parts concentrated HCl). Each sample was digested using a Multi-waveGo microwave digestion system (Anton Paar) with 4 mL concentrated HNO$_3$ (70%) and 2 mL concentrated HCl (36%). The sample underwent a 5-hour pre-digestion in HNO$_3$ prior to HCl addition and microwave heating. Digests were then diluted to 14 mL with deionized water, centrifuged if needed, and the clear supernatants were analysed by ICP-OES.

Variable-temperature X-ray diffraction (XRD) was performed using a Malvern Panalytical Empyrean 1 diffractometer equipped with an Anton Paar XRK 900 heating stage and a Cu Kα source (λ = 1.5418 Å). The electrode materials were scraped and dried inside the glovebox prior to further analysis. Measurements were conducted under flowing nitrogen. XRD patterns were initially collected at room temperature (RT), followed by measurements at 50 °C and then at 50 °C intervals up to 800 °C. At each temperature point, the sample was heated at a ramp rate of 15 °C min^{-1}, held isothermally for 5 minutes to ensure thermal equilibration, and then data were acquired. After reaching 800 °C, the samples were cooled back to room temperature at a controlled cooling rate of 50 °C min^{-1}, and final XRD measurements were collected to assess the structure after a thermal cycle.

Initial phase identification was performed using HighScore software (Malvern Panalytical), utilizing the PDF-4 database (International Centre for Diffraction Data, ICDD) to match experimental diffraction patterns to known crystallographic entries.[23] Rietveld refinements were carried out using the GSAS-II software suite, with refinable parameters including background, lattice parameters, profile coefficients, and phase fractions.[24,25] A systematic refinement strategy was employed, and efforts were made to maintain consistency in refinement conditions across the different compositions and temperature series wherever feasible.

Surface morphology and elemental composition were examined using a Zeiss Auriga Crossbeam FIB scanning electron microscope (SEM) and Hitachi TM4000Plus scanning electron microscope equipped with a Bruker SCU EDS detector. For SEM-EDS analysis, extracted electrodes were firmly attached to carbon adhesive tape on an aluminium sample stub with the original electrode surface facing the tape. The aluminium current collector was then carefully peeled off, exposing the bulk electrode material to the incident electron beam. This approach avoided collecting data on the SEI. Thermally treated samples were cooled to room temperature and lightly ground. Powdered samples were sprinkled onto carbon tape and mounted on aluminium stubs. Statistical EDS analyses were conducted on multiple particles per sample to evaluate Mn, Fe, and Ni distributions, as well as their atomic ratios in some cases relative to oxygen. Samples were handled under inert conditions to minimize air exposure.

25590 | Phys. Chem. Chem. Phys., 2025, 27, 25581–25592

This journal is © the Owner Societies 2025

Simultaneous TGA/DSC were carried out using a Discovery SDT650 (TA Instruments) instrument. Approximately 12–19 mg of dried cathode powder representing FC, PC, and FD states were placed in 90 μL alumina crucibles and heated from 30 °C to 800 °C at 15 °C min^{-1} under a nitrogen flow of 50 mL min^{-1}.

Mn K-edge XAS measurements were conducted on the MEX-1 Beamline at the Australian Synchrotron, employing a Si(111) double-crystal monochromator for energy selection. Cathode samples were mounted on sample holders and sealed with Kapton tape within an argon-filled glovebox to prevent air exposure. The incident X-ray beam was defined using upstream monochromatic slits, with slit apertures set to 4.5 mm and 4.0 mm. A knife-edge scan performed at the sample position during experimental setup determined the focused beam profile to have a full width at half maximum (FWHM) of 340 μm (horizonal) and 180 μm (vertical). Measurements were performed in transmission mode using 15 cm Ionitech gridded ion chambers filled with nitrogen gas at an absolute pressure of 2 bar. A Mn metal reference foil, positioned between the i1 and i2 ion chambers, served as an internal standard.

Fe and Ni K-edge XAS measurements were conducted on pressed pellets (13 mm diameter) prepared by homogenously mixing finely ground samples with 100 mg of cellulose binder. The total sample mass was optimized using the X-rayDB Python package to achieve adequate absorption (μ_{tot} = 1.0–3.5) and an appropriate edge step ($\geq$0.2), suitable for EXAFS analysis. XANES spectra were acquired in transmission mode using the easyXAFS 300+ spectrometer (easyXAFS LLC, Washington, DC, USA). Samples and reference standards were mounted on a stainless-steel sample wheel, and a helium-filled enclosure was used to minimize X-ray attenuation between the source, sample, and detector. Fe and Ni K-edge spectra were collected using a spherically bent silicon crystal analyzer (Si (110) for Fe and Si (551) for Ni), with a molybdenum anode X-ray tube serving as the source. Prior to data collection, the system was aligned through motor calibration and θ alignment scans. The X-ray tube current and voltage were adjusted to maintain detector deadtime below 30%. Ni and Fe metal foils were measured separately prior to sample acquisition and used to calibrate the initial energy scale. Additionally, blank measurements were performed under the same experimental conditions and subtracted from the raw data to remove background contributions.

Mn K-edge spectra were recorded across the energy range of 6339–6650 eV using the following step sizes: 10 eV below 6519 eV, 0.25 eV between 6519–6589 eV, 1 eV between 6589–7161 eV. The acquisition times were 0.5, 1, and 0.5 seconds per point for the pre-edge, XANES, and EXAFS regions, respectively, resulting in a total scan duration of approximately 5.3 minutes. Fe and Ni K-edge spectra were acquired over the energy ranges 7072–7297 eV (Fe) and 8293–8513 eV (Ni) with the following step scheme: 2 eV from 7072–7097 eV and 8293–8318 eV, 0.25 eV between 7097–7152 eV and 8318–8373 eV, 2 eV between 7152–7297 eV and 8373–8513 eV. Acquisition times were 1.5, 3, and 3 seconds per point, respectively, yielding a scan duration of approximately 14.8 minutes. The energy scale was calibrated using Mn, Fe, and Ni metal foils by aligning the peak of the first derivative of their respective K-edges to reference values: 6539 eV (Mn), 7112 eV (Fe), and 8333 eV (Ni). Data processing and normalization were carried out using the Athena software package within the Demeter suite, applying a normalization polynomial of order 3 for Mn and 2 for the Ni and Fe.[26]

Author contributions

B. D. K. K. Thilakarathna: investigation; writing – original draft; visualization; resources; methodology – conducted XRD, SEM and EDS including corresponding data analysis, prepared XAS samples, performed laboratory XAS data collection contributed to XAS, TGA, and DSC analysis, including data interpretation, and participated into experimental planning. Timothy A. Ablott: investigation; writing – review & editing – conducted TGA-DSC experiments, enthalpy calculations and data acquisition. Contributed to the final review and editing of the manuscript. Taren Cataldo: formal analysis; investigation; writing – review & editing – made major contribution to XAS data analysis and collaborated on TGA-DSC experiments and data collection. Contributed to the final review and editing of the manuscript. Pria Ramkissoon: resources; writing – review & editing – served as the MEX-1 beamline scientist at the Australian Synchrotron, ensuring beam stability. Contributed to the final review and editing of the manuscript. Govardhan Sontam: investigation; writing – review & editing – collected XAS data at the MEX-1 beamline and contributed to the XAS discussion; participated in the final review and editing of the manuscript. Neeraj Sharma: conceptualization; supervision; formal analysis; writing – review & editing – conceived the research idea, provided analytical guidance, mentored the project, and reviewed and edited the manuscript.

Conflicts of interest

There are no conflicts to declare.

Data availability

The data supporting this article have been included as part of the supplementary information (SI). Supplementary information is available. See DOI: **https://doi.org/10.1039/d5cp02777b**.

Acknowledgements

This journal is © the Owner Societies 2025

Phys. Chem. Chem. Phys., 2025, **27**, 25581–25592 | **25591**

References

1 P. T. Bhutia, S. Grugeon, A. El Mejdoubi, S. Laruelle and G. Marlair, *Batteries*, 2024, **10**, 370.

2 C. Didier, M. Guignard, M. R. Suchomel, D. Carlier, J. Darriet and C. Delmas, *Chem. Mater.*, 2016, **28**, 1462–1471.

3 J. Zhao, L. Zhao, N. Dimov, S. Okada and T. Nishida, *J. Electrochem. Soc.*, 2013, **160**, A3077–A3081.

4 W. Zuo, J. Qiu, X. Liu, F. Ren, H. Liu, H. He, C. Luo, J. Li, G. F. Ortiz, H. Duan, J. Liu, M. S. Wang, Y. Li, R. Fu and Y. Yang, *Nat. Commun.*, 2020, **11**, 3544.

5 S. Hwang, Y. Lee, E. Jo, K. Y. Chung, W. Choi, S. M. Kim and W. Chang, *ACS Appl. Mater. Interfaces*, 2017, **9**, 18883–18888.

6 P. Barpanda, G. Liu, C. D. Ling, M. Tamaru, M. Avdeev, S.-C. Chung, Y. Yamada and A. Yamada, *Chem. Mater.*, 2013, **25**, 3480–3487.

7 Y. Liu, Z. Wu, S. Indris, W. Hua, N. P. M. Casati, A. Tayal, M. S. D. Darma, G. Wang, Y. Liu, C. Wu, Y. Xiao, B. Zhong and X. Guo, *Nano Energy*, 2021, **79**, 105417.

8 B. D. K. K. Thilakarathna, U. Mittal, J. Peng, D. Brocklebank, H. E. A. Brand and N. Sharma, *Chem. Phys. Chem.*, 2025, **26**, e202400832.

9 Y. Xie, G.-L. Xu, H. Che, H. Wang, K. Yang, X. Yang, F. Guo, Y. Ren, Z. Chen, K. Amine and Z.-F. Ma, *Chem. Mater.*, 2018, **30**, 4909–4918.

10 A. Teng, Y. Zhang, L. Jiang, Y. Zhang, H. Dang, C. Wang, Z. Fang, Y. Liu, X. Wang, H. Li, W. Mei and Q. Wang, *J. Energy Chem.*, 2025, **103**, 838–849.

11 M. Jeong, H. Lee, J. Yoon and W.-S. Yoon, *J. Power Sources*, 2019, **439**, 227064.

12 Y. Xie, H. Wang, G. Xu, J. Wang, H. Sheng, Z. Chen, Y. Ren, C.-J. Sun, J. Wen, J. Wang, D. J. Miller, J. Lu, K. Amine and Z.-F. Ma, *Adv. Energy Mater.*, 2016, **6**, 1601306.

13 S. Komaba, N. Yabuuchi, T. Nakayama, A. Ogata, T. Ishikawa and I. Nakai, *Inorg. Chem.*, 2012, **51**, 6211–6220.

14 B. V. Kerr, H. J. King, C. F. Garibello, P. R. Dissanayake, A. N. Simonov, B. Johannessen, D. S. Eldridge and R. K. Hocking, *Energy Fuels*, 2022, **36**, 2369–2389.

15 D. Susanto, M. K. Cho, G. Ali, J.-Y. Kim, H. J. Chang, H.-S. Kim, K.-W. Nam and K. Y. Chung, *Chem. Mater.*, 2019, **31**, 3644–3651.

16 R. Samigullin, Z. Bobyleva, M. Zakharkin, E. Zharikova, M. Rozova, O. Drozhzhin and E. Antipov, *Energies (Basel)*, 2024, **17**, 3970.

17 B. Lu, D. Cheng, B. Sreenarayanan, W. Li, B. Bhamwala, W. Bao and Y. S. Meng, *ACS Energy Lett.*, 2023, **8**, 3230–3238.

18 E. Jakab and M. Blazsó, *J. Anal. Appl. Pyrolysis*, 2002, **64**, 263–277.

19 V. Boyko, Doctoral thesis, Institut. Werkstoffwissenschaften und -technologien, 2015.

20 P. U. Singare and A. N. Patange, *Int. Lett. Chem., Phys. Astron.*, 2014, **25**, 8–15.

21 S. Labus, A. Małecki and R. Gajerski, *J. Therm. Anal. Calorim.*, 2003, **74**, 13–20.

22 J. Lee, G. Choi, D. Kim and W. Kim, *Appl. Phys. Lett.*, 2000, **77**, 978–980.

23 S. N. Kabekkodu, A. Dosen and T. N. Blanton, *Powder Diffr.*, 2024, **39**, 47–59.

24 B. H. Toby and R. B. Von Dreele, *J. Appl. Crystallogr.*, 2013, **46**, 544–549.

25 P. Paufler, *Cryst. Res. Technol.*, 1995, **30**, 494.

26 B. Ravel and M. Newville, *J. Synchrotron Radiat.*, 2005, **12**, 537–541.

25592 | *Phys. Chem. Chem. Phys.*, 2025, **27**, 25581–25592

This journal is © the Owner Societies 2025